

To Appear in the *Astronomical Journal*

THE NICMOS ULTRA DEEP FIELD: OBSERVATIONS, DATA REDUCTION, AND GALAXY PHOTOMETRY

Rodger I. Thompson

Steward Observatory, University of Arizona, Tucson, AZ 85721

Garth Illingworth, Rychard Bouwens

Astronomy Department, University of California, Santa Cruz, CA 95064

Mark Dickinson

National Optical Astronomy Observatories, Tucson, AZ 85719

Daniel Eisenstein, Xiaohui Fan

Steward Observatory, University of Arizona, Tucson, AZ 85721

Marijn Franx

Leiden Observatory, Postbus 9513, 2300 RA Leiden, Netherlands

Adam Riess

Space Telescope Science Institute, Baltimore, MD 21218

Marcia J. Rieke, Glenn Schneider, Elizabeth Stobie

Steward Observatory, University of Arizona, Tucson, AZ 85721

Sune Toft, Pieter VanDokkum

Department of Astronomy, Yale University, New Haven, CT 06520

ABSTRACT

This paper describes the observations and data reduction techniques for the version 2.0 images and catalog of the NICMOS Ultra Deep Field Treasury program. All sources discussed in this paper are based on detections in the combined NICMOS F110W and F160W bands only. The NICMOS images are drizzled to

0.09/arcsecond pixels and aligned to the ACS UDF F850LP image which was rebinned to the same pixel scale. These form the NICMOS version 2.0 UDF images. The catalog sources are chosen with a conservative detection limit to avoid the inclusion of numerous spurious sources. The catalog contains 1293 objects in the $144 \times 144''$ NICMOS subfield of the UDF. The 5σ signal to noise level is an average $0.6''$ diameter aperture AB magnitude of 27.7 at 1.1 and 1.6 microns. The catalog sources, listed in order of right ascension, satisfy a minimum signal to noise criterion of 1.4σ in at least 7 contiguous pixels of the combined F110W and F160W image.

Subject headings: cosmology: observation — galaxies: fundamental parameters

1. Introduction

The NICMOS UDF Treasury observations were designed to complement and enhance the ACS optical UDF observations. They provide an extension in wavelength to $1.6\mu\text{m}$ and provide two additional bands which extend the rest band energy and morphology measurements to longer wavelengths. They also provide the potential for viewing objects at redshifts beyond 7.5 where Lyman line and continuum absorption quench the flux in the ACS bands. The additional wavelength coverage also helps distinguish between the influences of age, metallicity and extinction. As with previous deep field catalog publications (Williams et al. (1996), Thompson et al. (1999) and Beckwith et al. (2004)) this paper is intended primarily as a description of the observations, data analysis and source photometric properties rather than a scientific evaluation of the implications of the observations.

Due to the relatively small field of the NICMOS camera 3 used in this program ($51'' \times 51''$), only a subsection ($144'' \times 144''$) of the optical UDF was covered. This was done with a 3x3 tiling of the NICMOS images. The NICMOS images extend a few arc seconds beyond this subsection but at a significantly decreased signal to noise. All of the individual processed NICMOS images are available in the HST treasury archive (MAST¹) as are the raw images in the main HST archive.

The primary purpose of this paper is to provide a very detailed account of the data reduction steps used to produce the treasury images and catalog stored in MAST so that users are aware of the pedigree of the data and can reproduce the analysis if they wish. Other users may wish to alter the reduction steps if they prefer other choices than the ones made

¹http://archive.stsci.edu/prepds/udf/udf_hlsp.html

here. Finally we wish to convey the attributes and limitations of the catalog of sources. Users in particular who wish to extract the faintest sources from the data will want to use more aggressive extraction techniques than we have utilized in producing the treasury catalog.

2. Observations

The NICMOS observations in the UDF (HST GO/9803) are centered on the position $3^{\text{h}}32^{\text{m}}39.0^{\text{s}}$, $-27^{\circ}47'29.1''$ (J2000) at approximately the center of the ACS UDF observations (see image at <http://www.stsci.edu/hst/udf/parameters/#Pointing>). The images lie in a 3x3 grid with centers separated by 45 arc seconds. The grid centers are dithered by 5 arc seconds in a 4x4 square pattern tilted at 22.5 degrees to the x axis of the images to reduce the effect of intra pixel sensitivity variations. The tilt of the pattern also produces dithers that have fractional pixel offsets in the detector array.

The NICMOS UDF program consists of 144 orbits broken into two epochs: i) August 30, 2003 to September 14, 2003 and ii) November 2, 2003 to November 27, 2003. The scheduled start of observations in mid August 2003 was delayed by a safing of the NICMOS Cooling System (NCS) just prior to the beginning of observations. All reference files such as flats and darks were obtained subsequent to the safing event. The epochs are separated to enable the detection of SN Ia candidates and to provide enough SAA crossing free orbits for high sensitivity. The images in the two epochs are rotated by 90 degrees to accommodate the roll restrictions of the spacecraft. In the first epoch the y axis of the NICMOS camera 3 was oriented 40.925 degrees east of north, and in the second epoch 130.925 degrees east of north. These orientations are the same as the two ACS orientations in an effort to align the NICMOS and ACS images without the need for a rotation. The drizzled ACS images in MAST, however, were produced with the standard north up and east left orientation. The version 2 NICMOS treasury images supplied to MAST are also oriented with north up unlike the version 1 NICMOS image. The NICMOS version 2 images have been aligned with the ACS version 1 image so that researchers can utilize the complete set of ACS and NICMOS images without realignment or rotation, see § 3.7.

Each orbit contains a F110W and F160W band SPARS64, NSAMP = 24, 1344 second integration. Figure 1 shows the total response of the two bands, including the detector quantum efficiency. The F110W integration always preceded the F160W integration. Three orbits comprise a single visit with the location of the image specified by a POSTARG from the central reference position. It is possible that the F160W images from the first orbit of a visit may have received a small amount of earthshine in the last readout of the NSAMP = 24 readout sequence. This is due to the guide star acquisition time on the first orbit of

the visit which takes longer than the guide star reacquisition in the subsequent 2 orbits of the visit. No correction has been made in the Treasury images for this effect. The three by three grid was completed in three visits with each visit representing a 3 image strip stepped in the detector x direction. The visits were ordered to finish each 3 by 3 grid before starting another and always in the same order. This was done to maximize the time coverage for a supernova event, should one occur. After the initial delay due to the NCS safing all of the visits occurred in their expected order.

Subsequent analysis of the images indicated that the second half images were not an exact repeat of the first half images. In the second half 3 of the visits replaced a center image with an image on the right hand side of the 3 image strip. Tables 1 and 2 list the visits with T, C, B indicating top, center and bottom for the epoch 1 visits and L, C, and R indicating left, center and right for the 2nd epoch visits. These refer to left, right, top and bottom of the NICMOS images in their standard x and y orientations.

3. Data Reduction

Previous papers (Thompson et al. 1999; Thompson, Weymann and Storrie-Lombardi 2001; Thompson 2003) described details of the data reduction procedures for deep field NICMOS observations. Some of the procedures required revision for post NCS installation data. These changes and the provision of the reduced images as a public Treasury Program data products warrants a detailed description of the data reduction procedures even though some aspects have been covered in the publications cited above. All of the procedures utilize the commercial Interactive Data Language (IDL) ² software and the IDL based Fits List Calculator (FLC) (Lytle et al. 1999) software. These procedures were developed primarily by RIT and ES for previous NICMOS observations.

3.1. Basic Reduction

The initial steps in the data reduction take advantage of the nondestructive readout capability of the NICMOS detectors. NICMOS detectors are read out at specified intervals without erasing or altering the image. This ability allows several data reduction advantages not shared by CCD detectors. The SPARS64 read pattern with 24 samples provides readouts evenly spaced by 63.998 seconds after the first 2 samples that are spaced by 0.303 seconds.

²IDL is a registered trademark of Research Systems Incorporated, a Kodak company.

All of the images in the NICMOS UDF observations were taken in this mode. The steps described in this section are done automatically in batch processing with no interaction. This is roughly equivalent to the STScI pipeline processing.

3.1.1. First Read Subtraction

The first step in the data reduction is the subtraction of the image obtained in the first read from all subsequent reads. This step eliminates the KTC noise that is present in each of the individual photodiodes at the beginning of an integration. The number of reads carried through in the final processing is then 23 reads rather than 24 after this step.

3.1.2. Dark Current Subtraction

After the first read subtraction the dark current image is subtracted from each of the reads. This is a very important step as the NICMOS detectors have dark current images with very significant structure. This structure is larger in magnitude than the signal from most of the galaxies in the image. The dark images are constructed from integrations in exactly the same mode as the observations but with the cold blank filter in place. This step differs from the STScI pipeline that uses “synthetic darks” calculated from parameters developed during the operation of NICMOS (Mobasher et al. 2004a).

3.1.3. The UDF NICMOS Dark

The NICMOS UDF dark is a median dark image obtained from dark integrations taken during the earth occultation period in each of the orbits assigned to the NICMOS UDF program. Operational constraints prevented dark integrations on 2 orbits but the remaining 142 dark integrations were used to construct the median images. There is a median dark image for each read constructed from the medians of all of the dark images for that particular read.

Between visit 34 and visit 35 of the 48 visits in the NICMOS UDF program, the temperature set point on the NCS was reduced by 0.1 K to compensate for the warmer conditions encountered during the period when the earth’s orbit is closest to the sun. There was concern that this set point change would alter the nature of the NICMOS darks since it is known that the darks are temperature sensitive. Comparison of a median of the darks taken before the set point change with the median darks taken after the set point change did not reveal any

differences above the noise level in the observations. The NICMOS UDF dark was therefore constructed from the median of all of the darks before and after the set point change.

3.1.4. *Warm Pixels*

In the NCS era the NICMOS detectors operate at a significantly warmer temperature than the previous operation with solid nitrogen cryogen. There are several advantages to the warmer detector temperature but a disadvantage is an increase in the number of “hot” and “warm” pixels. Hot pixels are pixels with a dark current high enough to reach the nonlinear response region in a 1000 second integration. These pixels are included in the list of bad pixels described in § 3.1.9. More difficult cases are the warm pixels that have elevated dark current but not elevated enough to become nonlinear in a normal integration. These pixels can be corrected through the dark image subtraction for most types of integrations. The degree of elevation, however, is very temperature dependent, and will vary over the normal range of temperature variations inherent in the NCS operations. The elevated dark current is in many cases much larger than the signal encountered in faint galaxies.

The warm pixels contribute noise in two ways. First is the normal Poisson statistics inherent in a steady dark current and the second is incomplete removal when the dark current varies from the median dark current measured by the NICMOS UDF dark. The presence of these varying warm pixels altered the previous data reductions in two ways. The first was the introduction of a more aggressive bad pixel list for the UDF observations and the second was the introduction of post processing procedures to detect the presence of warm pixel signals and to separate them from true sources. These procedures are described in § 3.6.

3.1.5. *Linearity Correction*

During thermal vacuum testing prior to launch and in cycle 7 the linearity of each pixel was measured. The point at which nonlinearity set in and coefficients for a polynomial fit after that point were determined for every pixel. In the linearity correction stage the signal of every pixel is checked to see if it is in the nonlinear range. If it is above the linear range its signal is corrected using the determined coefficients of the polynomial fit. If it is in the signal range that is deemed uncorrectable it is marked as saturated and only the reads occurring before saturation are used in the analysis. New coefficients are being determined for post NCS operation. However, none of the galaxies in the UDF reached signal levels requiring

correction therefore linearity is not an issue in this analysis.

3.1.6. Cosmic Ray Removal

A cosmic ray event produces a sharp jump in signal intensity in the first readout after the event. Most events do not saturate the pixel and subsequent readouts continue to monitor the incident flux. At this point in the analysis the readouts are stored as delta signal levels between each readout. The signal “ramp” is reconstructed by adding the deltas together. The first step in cosmic ray detection is a linear fit to the signal ramp, which will be a poor fit to the data if there is a cosmic ray jump. The residuals to the fit will be increasingly negative with a sharp transition to positive after the event. The cosmic ray detection procedure looks for the negative to positive transition as a signature of a cosmic ray hit. If it detects a residual transition above the level expected from noise it removes the delta signal between the two readouts before and after the event, recalculates the signal ramp and fits a new linear solution.

The cosmic ray procedure rechecks the ramp to see if there was another cosmic ray hit and removes the proper delta signal if one is detected. If there is still a detectable cosmic ray signature after the second refit the pixel is marked as bad and no further correction attempt is made. If the signal is saturated after the cosmic ray hit only the signal obtained before the event is used in the analysis. The final recorded signal is the value of the slope of the linear fit to the signal ramp in adus per second. Cosmic ray hits that occur in the 0.3 seconds between the first and second read are detected as fits that do not intercept zero, recalling that the first read is subtracted from second so that the second read is the first point in the ramp. These hits do not affect the calculated slope but are marked as cosmic ray hits in the data quality array discussed later.

3.1.7. Quadrant Bias Correction

Each quadrant of the NICMOS detectors has a separate output amplifier to transmit the analog signal to an A/D converter. This was done to prevent the loss of an entire detector array if there was a failure of an output amplifier. As a side effect of this design decision a small DC bias offset can occur between the 4 detector quadrants. Although the offset is small, the effect is significant relative to the faint galaxy signals in the UDF and can cause unreliable outputs during the drizzle process. Since there is significant sky background from the zodiacal light it is difficult to determine the offset amount from a simple inspection of

the image.

The quadrant bias is removed via a procedure based on the bias removal procedure developed by Mark Dickinson as part of the STScI NICMOS team (Mobasher et al. 2004b). The procedure utilizes the flat field imprint produced on the DC signal by the flat field correction process. Any flat DC bias will be modulated by the variations in the flat field. The process successively subtracts a DC bias from each quadrant before it is flat fielded, applies the flat field and then picks the bias subtraction that produces the minimum variation in the quadrant. The variation in the quadrant signal is measured by a gaussian fitting to the histogram of pixel values in the images. To avoid any residual corner glow from the amplifiers or other quadrant boundary anomalies only the quadrant region that is at least 20 pixels from the quadrant edges is used to determine the quadrant bias. Bad pixels are also masked out to prevent them from dominating the variation signal. The output of variations from each bias correction is fit by both a second order polynomial and by 5 point smoothing of the output. In the cases encountered in the UDF images they are essentially identical. The minimum variation bias correction is selected as the minimum of the smoothed output.

Both positive and negative bias are subtracted as the bias can have either a positive or negative value. The bias subtraction used biases between -0.15 and 0.2 adus per second incremented in 0.001 adus per second. The procedure returns a warning if any bias corrections do not find a minimum in the provided range of biases. All of the UDF quadrant images had minimums within the range of biases in the procedure. An example of the gaussian width versus subtracted bias is shown in Figure. 2. Visual inspection of the images before and after background subtraction confirmed that there were no detectable remaining quadrant bias offsets. The procedure would be unnecessarily time consuming for images where the objects were significantly brighter than the offsets and might not work in images where the width of the pixel signal histograms are dominated by source variations rather than noise. Neither is the case for the UDF. In reality the IDL code for this procedure actually performs both the flat fielding and bad pixel correction. These procedures, however, are discussed individually in the following sections.

3.1.8. Flat Fielding

NICMOS flat fields are created internally. The “beam steering mirror” internal to the instrument lies at a optical pupil and is used to correct the spherical aberration of the HST primary. It can be illuminated from behind and the reflective coating of the mirror was adjusted to be about 0.01% transmitting producing an illuminated pupil for flat fielding. Flat fields are produced at regular intervals during operation in all filters of each camera.

We used F110W and F160W camera 3 flat field observations created on Sept. 9, 2003 from proposal 9640. The flat fields are analyzed in the identical manner as described in the preceding steps. The STScI reference flat fields were not used in this analysis because they were based on flat fields observed previous to the NCS safing event.

One of the effects that the flat field corrects is a slight vignetting along the lower edge of camera 3. For two reasons this correction was not effective in the UDF fields. First, the net effect has two components, vignetting of the incoming astronomical flux and emission from the vignetting component which is thought to be the edge of the mount for the field division mirror for camera 3. For bright sources the vignetting is the dominant effect and the flat field properly corrects the field. For very faint images, such as the UDF, emission can be a significant component which varies due to the natural temperature variations in the aft shroud. Second, variations in geometry due to temperature changes can affect the degree of vignetting. Again the effect is slight for bright sources but can be significant for the UDF signal levels. For these reasons the lower 20 rows of all UDF images were masked off in the drizzle procedure described in section 3.7.

3.1.9. Bad Pixel Correction

Bad pixels are defined as pixels with quantum efficiencies less than 10% of the average QE or with dark currents high enough to reach nonlinear signal levels in 1000 seconds or less. In the post NCS era the list of bad pixels has increased over the cycle 7 listing due to the higher temperature of the detector creating more high dark current pixels. Pixels which satisfy neither criterion but are highly variable in their dark current were also added to the list. All bad pixel signals are replaced with the median of the eight pixels surrounding them. In the case of adjacent bad pixels that number is reduced by the number of adjoining bad pixels. All bad pixels are listed in the data quality array which is an extension of the image or SCI array. Table 3 gives the decimal codes for each of the steps described above. They are each a single, different, binary bit, so each combination of actions performed on a pixel has a unique output code. Note that only a few of the 16 bits available for pixel actions are used in this analysis. A full set of data quality codes can be found in the NICMOS Handbook but only the ones listed here are used in the NICMOS UDF Treasury data. Even for the codes used they may in many cases differ from the codes returned by the STScI pipeline analysis. As an example, the lists of bad pixels differ between the pipeline analysis and the analysis described here. Note that the data quality extensions only exist for the individual NICMOS UDF images. The drizzle procedure does not preserve these codes since many input pixels contribute to a single drizzled output pixel.

3.2. SSA Persistence Correction

The program planners at STScI were careful to schedule the NICMOS UDF observations in orbits that were not impacted by SAA passages. None of the NICMOS UDF images required any correction to remove SAA persistence.

3.3. Earthshine Detection

As mentioned in § 2 the last read of the first orbit in a visit may have encountered increased earthshine due to the longer period of delay in a guide star acquisition rather than reacquisition. This would only affect the F160W images as the readout sequence was always F110W and then F160W. We tested for this effect by plotting the median of the delta increase in the F160W images as a function of readout. In a few cases we saw a detectable rise in the last readout of the first orbit in a visit. The effect appeared minor enough that no correction was attempted.

3.4. Background Subtraction

The primary background source in the UDF is zodiacal emission which is relatively uniform across the small UDF field of view. A median image of all of the images in the F110W and the F160W filter determines the background for that filter. The background is simply subtracted from each image in the proper filter. The median image is extremely smooth with no indication of any residual source structure. This is similar to the results in the NHDF Thompson et al. (1999) where the spacing between images was much smaller than in the UDF. Since the zodiacal backgrounds can be time dependent the first epoch and second epoch background subtractions were done independently.

3.5. Residual Bias Correction

The removal of quadrant biases and the background subtraction should result in an image that has a median value of nearly zero since most of the pixels in the image are not in sources that are above the noise level. The minimums of the quadrant bias curves in Figure 2, however, are rather broad. To compensate for this each quadrant of every image was set to zero bias. The bias was determined from the median of the portion of the quadrants which is 40 rows and columns away from the edge to avoid any contamination from residual corner

glow or uncorrected vignetting. Any detected bias was subtracted from the entire quadrant to produce a zero bias image. Inspection by eye of the zero bias images did not find any detectable quadrant offsets.

3.6. Warm Pixel Correction

A new effect encountered in the NICMOS UDF images is warm pixel variation. At the higher operating temperature of the NCS cooling system, the NICMOS detectors have more warm pixels than during the cycle 7 operation with solid nitrogen cryogen. A warm pixel is defined as a pixel with an elevated dark current which is not high enough to be declared a bad pixel by the criteria defined in § 3.1.9. For most applications warm pixels are adequately corrected by dark subtraction but for the UDF they present two problems. The first problem is that their dark current is temperature sensitive and the NCS has slight temperature variations within an orbital cycle and within a 24 hr day due to power cycles in HST operation. The variation is small but is significant relative to faint UDF sources. The second problem is that the Poisson noise of the signal at the end of an integration is also significant relative to a UDF source. The individual images have single or sometimes double pixels with signal levels of either positive or negative high contrast relative to the surrounding pixels from the warm pixel effect.

Warm pixels are identified by their contrast with neighboring pixels. The PSF of a point source centered on a pixel provides a maximum contrast for a real source. Pixels with contrasts significantly greater than this are due to warm pixels. The contrast was computed for each pixel compared to the 8 pixels adjacent to the pixel. A pixel is set equal to the median of the 8 pixels if 3 conditions are met; i) its value is higher than the 3σ noise value in the image, ii) its value is higher relative to the median of the adjacent pixels than a preset contrast value and iii) the value of the surrounding median is less than a preset number of standard deviations. The last condition prevents peak clipping on point objects. The contrast values were set to 6.0 for the F160W image and 8.0 for the F110W image which has a narrower PSF. The standard deviation limits were set to 2.5 for the F160W images and 2.0 for the F110W images. Any corrected pixel has the bad pixel flag set in the DQ image extension so it can be identified.

3.7. Drizzle Procedure

The treasury mosaic images were produced using the DRIZZLE procedure with context images (Fruchter and Hook 2002). The offsets for the NICMOS images were determined by registering the NICMOS F110W images onto the ACS F850LP UDF image in the HST archive which has a north up orientation and 0.03'' pixel scale. The significant overlap between the two filters greatly reduces any errors due to color dependent morphology, however, see § 3.7.3 for an assessment of the accuracy of the alignment. The NICMOS F160W images which always immediately followed the F110W images in an orbit were assumed to have the same offset as the F110W images preceding them. The ACS image was reduced to 0.09'' pixels by a simple 3x3 pixel addition of the image. Individual NICMOS F110W images were then produced with a drizzle PIXFRAC parameter of 0.6 and a SCALE parameter of 0.09/0.202863 to produce 0.09'' output pixels. The denominator in the scale factor is the pixel size of the distortion corrected NICMOS pixel. The geometric distortion coefficients Bergeron (2004) are given in Table 4. These coefficients are the constants for a cubic distortion correction of the form

$$x_{dist} = a1 + a2 \times x + a3 \times y + a5 \times x \times y + a6 \times y^2 + a7 \times x^3 + a8 \times x^2 \times y + a9 \times x \times y^3 \quad (1)$$

and an identical equation in b coefficients for the y position that governs the placement of the pixels. Compared to other HST instruments the correction is relatively small. The main component is the difference in plate scale between the x and y directions due to a slight tilt in the camera 3 focal plane relative to the plane of the detector. The tilt is due to the curvature of the focal plane. Each 0.09'' NICMOS was rotated to a north up orientation using the ORIENTAT value in the image header.

A three step process provided the positions of each F110W image relative to the ACS F850LP image. The first step was to shift the NICMOS images to the positions indicated by their World Coordinate System (WCS) position in the headers. The second step was a non-interactive chi squared minimization of the differences between the bright objects in the NICMOS image and the nearest corresponding bright ACS object. The ACS positions were determined with SE in the ABSOLUTE mode with the threshold set at 0.03 ADUs per second. Positions in the NIMCOS images were also determined with SE in ABSOLUTE mode with the threshold set at 0.01 ADUs per second. Both of these thresholds are quite bright to insure a low source count per area. This made the likelihood of wrong object matching low. The shifts were limited to plus or minus 10 pixels in the X and Y directions in single pixel steps. The average position shift in this step was on the order of 2 to 3 0.09'' pixels. The final shifts were determined by a similar chi squared minimization of interactively

selected NICMOS objects. Usually three objects were selected based on compact size and sufficient signal to noise. Whenever fully visible in a NICMOS image, the star near the center of the image was used as one of the objects. The more eastern star image appears to have contamination due to a faint nearby object visible in the ACS images. Shifts in this step were limited to plus or minus 1 pixel in 0.1 pixel steps. The average position adjustment in this third and final stage was 0.2 to 0.3 $0.09''$ pixels. These final positions were then used as the input to the drizzle procedure.

3.7.1. Individual Image Masking

The F110W and F160W images each have a general mask used in the drizzle process. The masks mask out the bottom 20 rows of the image to eliminate the partially vignetted region at the bottom of camera 3. They also mask out a portion of the upper right hand corner of camera 3 where there is an area of rapidly changing quantum efficiency. In addition they also mask out the known bad pixels and areas where some particles, termed grot, cover detector pixels. The large number of dithered images greatly reduces the impact of the masked areas. The masks are available in the STScI NICMOS UDF Treasury version 2.0 archive in MAST. Several of the images had artifacts such as satellite passage streaks that required masking. Individual masks were made for 20 F110W images and 31 F160W images. Table 5 lists the masked images. The masks are contained in the NICMOS version 2.0 Treasury submission.

3.7.2. Cosmic Ray Persistence

A few of the masks remove spurious objects created by cosmic ray persistence. If a cosmic ray hit before the start of an integration produces a shower of particles, cosmic ray persistence can give a resolved source that appears in the first F110W image after the hit and more weakly in the following F160W image. This exactly mimics a high redshift galaxy. The ACS image has no signal and the F110W-F160W color is blue. The signature of this spurious event is that the source only appears in one set of F110W and F160W images. All of the NICMOS sources that did not have ACS counterparts were inspected in each image. Two spurious cosmic ray persistence sources were found and masked out (see also § 7.4).

3.7.3. Point Spread Functions

Unlike the deep NICMOS observations in the NHDF, the HST secondary mirror was not adjusted to bring the camera 3 images into sharp focus. The photometric gain was not considered high enough to request the adjustment which would have put the parallel ACS images significantly out of focus. The PSF at the focal plane of camera 3 is therefore broader than the diffraction limited PSF observed by NICMOS cameras 1 and 2. To determine the PSFs of the UDF images two measurements were performed. The first was to measure the PSF of the bright star at $x = 1897.26$, $y = 1610.34$ with Gaussian fitting. The second bright star at $x = 1246.12$, $y = 1420.42$ appears to be double with a faint companion. The second measurement involved 42 camera 3 images in F110W and F160W of the photometric calibration star P330-E taken after the NCS safing event. These were part of the Prop. 9995 calibration program of Mark Dickinson. These images were drizzled in the same manner as the UDF images. The PSF of the drizzled F110W and F160W images were measured by the same Gaussian fitting as for the UDF stellar images. The results are listed in Table 6 which gives the measured major and minor axis FWHM values. Table 6 also gives the results of performing the same exercise on synthetic images produced with the Tiny Tim software (Krist and Hook 2004) for the camera 3 focus utilized in the UDF observations. The Tiny Tim and calibration star PSFs agree quit well but the measured UDF stellar values are between 0.06 and 0.1 arc seconds wider. This may reflect the accuracy of the mosaic position calculations. The widths measured in an independently reduced image (see § 7.4) are very similar to our UDF image widths. Any researcher that requires extremely accurate object shapes, such as for weak lensing, may wish to go to the original single images for size and shape measurements. Those researchers should apply the geometric distortion corrections listed in Table 4.

4. Image Size and Weight

The full drizzled image does not have a uniform integration time over the image. In particular the edges of the image have only one integration as opposed to the average 16 integrations for the interior of the image. The full drizzled image has a size of 3500 by 3500 pixels, the same size and orientation as the ACS images reduced to $0.09''$ pixels. Experience with the NHDF images indicated that source extraction in regions with less than half of the average integration time was not profitable except in special cases where a particular object near the edge of the total image required analysis. Users of the treasury image should be aware that the edges of the image have roughly a $\sqrt{2}$ lower signal to noise than the central regions. The exact weight for all pixels is given by the weight images included in the treasury

archive. There are some regions where the images overlap that have much higher integration times. Users who need a uniform selection criterion for analysis should be aware of these differences in weight.

5. Source Extraction

Source extraction in the science image was performed with the source extraction program SExtractor (SE) version 2.3 (Bertin and Arnout 1996) in the dual image and rms image mode. The source extraction includes the 4 ACS UDF images as well as the NICMOS images. The ACS extractions provided the source reality check described in § 7.3 and are included in the treasury catalog.

5.1. Noise

Figure 3 shows the histograms of all of the pixel values in the F110W and F160W image. The majority of the pixels are well fit with a gaussian centered on zero. The offsets from zero are 7×10^{-5} ADUs/second for both images. The positive tail deviating from a gaussian is the contribution from the true sources in the field. The width of the gaussian fit is an indicator of the noise. The gaussian fit gives noise levels of 3.5×10^{-4} ADUs per second for the F110W image and 3.7×10^{-4} ADUs per second for the F160W image. This corresponds to 0.55 and 0.58 nanojanskys respectively. This is an underestimate of the true noise as is partially indicated by the excess over the gaussian on the negative side of the fit. The drizzle procedure is known to introduce correlation to the noise (Fruchter and Hook 2002). Fruchter and Hook (2002) give an expression for the noise increase factor which gives a factor of 1.8 for the drizzle PIXFRAC and SCALE parameters used in the images. This yields 1σ noise values of 1.0 and 1.2 nanojanskys per pixel.

Figure 4 shows the histograms of the signals in a densely packed grid of apertures of the same diameter as the three apertures, 6, 11 and 17 pixels, used in the source extraction. The 175x175 grid is regularly spaced on 20 pixel centers to provide 30,625 apertures. Most of these do not contain sources but the positive tail in Figure 4 indicates apertures with positive source flux. The large number of apertures that fall off the NICMOS image are not included in the analysis. The histograms are roughly Gaussian shaped but only the 6 pixel aperture histogram has an easily measurable FWHM. The 1σ noise derived from the FWHM is 3.7×10^{-3} ADUs per sec for the F110W image. Similar results were obtained for the F160W image. The expected noise from the individual pixel noise described above,

including the factor of 1.8, is 3.5×10^{-3} which is comparable to the measured value. To the degree that the aperture noises are truly Gaussian distributed, this indicates that factor of 1.8 is a reasonable figure to account for the correlated noise and that the aperture noise is approximately equal to the square root of the number of pixels in the aperture times the individual pixel noise. The measured aperture noise in Janskys from the histogram is 5.8×10^{-9} which is equivalent to an AB magnitude of 29.5 for the $0.54''$ diameter aperture. The 5σ AB magnitude is 27.7 which we will take as the appropriate value independent of source noise. In observations of the NHDF-S Labbé et al. (2003) with ISAAC on the VLT found 1σ aperture noises of 28.6 and 28.1 for the J and H bands with a $0.7''$ diameter aperture which gives 5σ values of 26.7 and 26.2. The minimum number of contiguous pixels for a real source is set to 7 in the extraction procedure. The 5σ noise for a point source detection is then the noise in the 7 pixel aperture which gives AB magnitudes of 30.35 and 30.15 for the F110W and F160W filters respectively.

5.2. Detection Image

SE in the two image mode uses a detection image to determine the position and extent of sources. The individual image source extraction is then performed on exactly the same positions and regions determined from the detection image. The SE parameters regarding source geometry such as area and ellipticity are determined by the detection image. The detection image for the treasury catalog is the simple sum of the F110W and F160W science images. Even though it is the sum of two images, the detection image has a significantly lower signal to noise than any of the ACS UDF images except for sources that are extremely red. Users that are interested in the NICMOS limits on faint ACS UDF sources should use the ACS images as the detection image to perform the source extraction on the NICMOS images. On the other hand very red sources may appear only in the NICMOS images. Since we wish to provide an infrared catalog we chose to use the NICMOS images for extraction. Note that by combining the two NICMOS images there is a bias against the very reddest sources that might only appear in the F160W image.

5.3. RMS Image

SE utilizes a rms image to determine the detection limit of a pixel signal when operating in the RMS mode used in the treasury version 2.0 catalog. The drizzle procedure produces an observation time weight map that measures the total integration time for every pixel but the weight map does not take into account the large variations in quantum efficiency

over the face of the NICMOS detector array. To account for the QE variations, the F110W and F160W flat field images were drizzled in exactly the same way as the UDF images, utilizing identical masks. Note that the flat field images are the multiplicative flats used in the normal image reductions. As such they are high where the signal is low and vice versa. All subsequent post drizzle procedures that were applied to the science images were also applied to the drizzled flat images. Next the median of the drizzled flat images was set to one and multiplied by the standard deviation determined in § 5.1, adjusted by the correlation parameter of 1.8. These images were then added together as the square root of the sum of the squares to form the rms image for the detection image supplied to SE. This rms image properly represents the differences in QE across the detector and the mapping of the differences onto the final science image. The individual F110W and F160W rms images were retained for use in the source extraction described below. The ACS rms images were assumed to be uniform and equal to the standard deviations found in § 5.1 for the individual ACS images. The individual filter rms images form the basis of the magnitude and flux errors returned by SE.

5.3.1. RMS Image Adjustments

Visual inspection of the detection image and the individual NICMOS drizzled images revealed small areas where there were clearly higher regions of noise or residual spurious artifacts. These are usually regions of “cross hatched” noise or small irregular regions of a few pixels with boundaries too sharp to be real sources. Even though areas such as these were masked in the original images, the drizzle process can produce additional areas due to rebinning process. Rather than removing these regions from the images, the rms images were adjusted to guarantee that they were not used in the source extraction. The pixel regions with adjusted rms values are given in a table supplied with the version 2 submission. These regions can also be identified in the rms images themselves where they have been set to 9.999. This procedure preserves the ignored areas in the images so that they can be evaluated by other researchers if they wish, just as the individual images, before masking, can be retrieved from the archive. Areas outside of the observed regions were set to very high rms values on the order of 500. to 800.

5.4. Extraction parameters

SE’s source extraction process is controlled by a configuration file that gives the parameters for source extraction. Some of the configuration parameters used in the version

2.0 treasury source extraction are given in Table 7. The full configuration files used in the extraction are included in the Treasury NICMOS UDF version 2.0 submission to MAST. The parameters include a detection threshold of 1.4σ and the minimum number of contiguous pixels for a true source set to 7. Note that these parameters discriminate against faint point sources.

Although not evident from the documentation, SE runs in a dual rms image mode. In this mode two rms images are supplied in the WEIGHT_IMAGE parameter. The first image is the rms image for the detection image and the second is the rms image for the extraction image which is the UDF image in each of the individual filters. The second rms image does not influence the source selection but determines the error values returned by SE.

The photometric zero points in AB magnitude are 23.41 (F110W) and 23.22 (F160W). The extraction parameters were adjusted to produce a clean extraction of sources with a goal of no erroneous detections in the high signal to noise regions of the image. This produces a relatively conservative catalog given the range of weighting over the image. Visual inspection of the image indicates that there are real sources that have been missed by the extraction process. More aggressive extraction parameters pick up these sources but also begin to find sources of doubtful reality. (See § 7.) Users who wish to have a more aggressive extraction can use our parameters as a starting point and adjust them to produce the required level of extraction. Our parameters produced 1293 extracted sources.

6. Catalog Construction

All of the output values listed in the treasury catalog are outputs from SE with no editing. The source order has been rearranged to be in order of increasing right ascension. To maintain correspondence with the segmentation images that were returned by SE, the original source identification numbers assigned by SE are given in the catalog. Ten of the sources detected by SE are not included in the catalog as described in § 7.3 leaving 1283 of the 1293 detected sources.

Each source has 90 entries, therefore, we do not include the table in the paper. The catalog is available at the STScI MAST site containing the NICMOS version 2.0 high level science products. That catalog is a comma separated text file. Columns 1-2 contain the ID number and the ID number of the associated source in the version 1 I band based ACS UDF catalog. The associated ACS source is the closest source to the catalog source. If there is no ACS source within 0.3 seconds of the NICMOS source a 0 entry is made in column 2. Column 3 gives the distance to the associated source in arc seconds and column 4 gives ID

number of the source in the SE produced segmentation image which is also provided in the MAST archive. If a version 2 catalog of ACS sources is produced we will attempt to provide a version 2.1 catalog with the new ACS source identifications included.

Columns 5 and 6 give the x and y positions in pixels of the source in the version 2.0 treasury image. Columns 7 and 8 are the RA and DEC positions in degrees while columns 9 and 10 are the RA and DEC position in traditional nomenclature. Columns 11-28 give the aperture AB magnitudes of the source. The 3 aperture magnitudes of the ACS F445W band are listed first followed by the remaining ACS and NICMOS bands in order of wavelength. Columns 29 through 34 list the isophotal magnitudes and columns 35 through 40 list auto magnitudes returned by SE in the same order.

Column 41 lists the number of pixels associated with the source in the SE segmentation image. Columns 42 through 47 list the FWHM in each band. Column 48 lists the position angle of the source returned by SE. Column 49 lists the flag value returned by SE. No sources have been removed from the catalog on the basis of the value of the SE error flag. Columns 50-55 list the XPEAK, YPEAK, XMIN, YMIN, XMAX, and YMAX values returned by SE. The source is contained in a box defined by the minimum and maximum x and y values. Columns 56 and 57 give the ellipticity and elongation of the source returned by SE. Column 58 contains the 0.6'' diameter aperture AB magnitude of the F160W band.

Columns 59-76 contain the aperture fluxes in the same order as the aperture magnitudes. The fluxes are in ADU/sec. The NICMOS gain is 6.5 electrons per ADU. Columns 77 through 82 list the isophotal fluxes and columns 83 through 88 list auto fluxes returned by SE. Columns 89 and 90 are the ISOAREA and ISOFAREA values returned by SE.

6.1. Mini-Catalog

To be consistent with the ACS UDF submissions we have also constructed a mini-catalog of the sources, part of which is included in the printed version of the paper. The whole catalog is available in the electronic version of the paper. The catalog appears in Table 8. There are some differences relative to the ACS catalog available in MAST. First the catalog is ordered in RA with the associated ACS source ID and the segmentation ID in columns 2 and 3. The x and y positions followed by the RA and DEC in degrees are in columns 4-7. Next are the position angle, ellipticity, half radius, FWHM and stellarity in columns 8-12. These are followed by the isophotal magnitude, isophotal magnitude error, and signal to noise for the 4 ACS and 2 NICMOS bands starting with the ACS F435W and ending with the NICMOS F160W band. The signal to noise is the ratio of the isophotal

flux to the isophotal flux error returned by SE. The last entry in the table is the value of the error flag returned by SE. As in the larger table there has been no effort to remove sources based on the SE error flag. Due to space constraints only the first few columns of the table are present in the printed version.

7. Source Reliability

Although the extraction parameters were adjusted conservatively, independent assessments of the source reliability are required. The following analyses and tests were performed to judge the reality of the catalog sources.

7.1. Signal to Noise Values

The source extraction program, SE, returns flux errors as well as fluxes. Figure 5 shows the measured signal to noise values for the faint end of the catalog. The ratio of the isophotal flux to isophotal flux error is plotted versus isophotal magnitude. There is significant scatter in the values as expected. The average magnitude for a signal to noise ratio of 5 appears to be around an isophotal magnitude of 28.4 significantly fainter than the aperture test value of 27.7 found in § 5.1. The details of how SE computes its flux errors are not immediately obvious so the value of 27.7 will be used. The rms images supplied to SE were multiplied by 1.8 for the expected correlation due to drizzling so that should not be an explanation for the difference.

7.2. Negative Image

As a check on noise induced sources we ran the identical extraction procedure on the negative of the original source detection image. The procedure produced no detections from the negative image. This indicates that the number of sources produced by noise is very low.

7.3. Comparison with the ACS images

The presence of the much higher signal to noise ACS images provided a second test of source reliability. We checked for catalog sources that had ACS F850LP 0.6" aperture diameter AB magnitudes fainter than 29.5. The smallest aperture was chosen to minimize

flux from overlapping sources. We identified 22 sources out of the total 1293 sources that matched that criterion. Two of these sources are in the high redshift source list of 5 sources described by Bouwens et al. (2004) where the Lyman break occurs to the red of the ACS cutoff. Bouwens et al. (2004) used a more aggressive source extraction which accounts for the extra three sources in their analysis. The remaining 20 sources fell into 3 categories. The first were legitimate sources with ACS F850LP flux below the limit but clearly there under visual inspection. There are 10 sources in this category. The second category is sources with clear flux in only the F160W band. There are 2 sources in this category. The remaining 8 were sources that appear to be noise artifacts by a subjective visual analysis. The 10 objects in the last two categories do not appear in the catalog even though the 2 sources with only F160W flux may be real.

7.4. Comparison with an Independently Generated Image

The NICMOS UDF images were independently reduced at STScI by Massimo Stiavelli, Bahram Mobasher and Louis Bergeron. They very graciously provided these images for comparison with our reductions. Inspection of these images revealed two objects in our images that were the result of cosmic ray persistence (See § 3.7.2). These objects were masked out in the individual image they appeared in for the final drizzle run. One NICMOS object that does not have an ACS counterpart, object 937, Bouwens et al. (2004) UDF 818-886, does not appear in the Stiavelli, Mobasher and Bergeron image. Inspection of our individual images indicates that no single image contributed the majority of the flux as would be expected for a cosmic ray persistence event. The object appears faintly in several of our individual images in both filters. To date we have not been able to resolve why this discrepancy exists. Users of the catalog should be aware of this discrepancy, particularly because this source satisfies the criteria for a galaxy at a redshift greater than 7.

8. Conclusions

Although this is a description of the data and techniques utilized in constructing the NICMOS UDF Treasury Version 2.0 catalog, it has been traditional (Williams et al. (1996), Thompson et al. (1999)) to show a number magnitude diagram from the data. Figure 6 displays the number magnitude diagram in AB magnitudes for the NICMOS F160W sources in the Ultra Deep Field. The vertical error bars are calculated from number statistics only. Other errors such as incompleteness, source noise, and large scale structure are not included. The fall off at AB magnitudes greater than 27 is certainly due to incompleteness, partially

due to the conservative source extraction parameters used in the construction of the Treasury catalog. Note that the magnitudes are aperture magnitudes in the smallest, $0.6''$, aperture. For comparison the F814W data from the NHDF (Williams et al. 1996) are also plotted. The agreement is good, with the F160W plot possibly having a slightly steeper slope, opposite to what was observed in the NHDF (Thompson 2003).

9. Acknowledgments

We are extremely grateful to Massimo Stiavelli, Bahram Mobasher and Louis Bergeron for pointing out objects in our reduction that did not appear in their independent reduction of the same data and for providing one of us (RIT) with the images for detailed comparison. We are grateful to all of the personnel at STScI, and in particular Beth Perriello, who worked very hard to make the NICMOS UDF observations a success. This task was made even more difficult by the NCS safing that delayed the beginning of the observations. This article is based on data from observations with the NASA/ESA Hubble Space Telescope, obtained at the Space Telescope Science Institute, which is operated by the Association of Universities for Research in Astronomy under NASA contract NAS 5-26555. The individual researchers are funded in part by NASA Grant HST-GO-09803.01-A-G from the Space Telescope Science Institute. ST received support from the Danish Natural Research Council.

REFERENCES

- Beckwith, S.V.W. 2004, in preparation.
- Bergeron, L. 2004, private communication.
- Bertin, E., and Arnouts, S. 1996, *A&A*, 117, 393.
- Bouwens, R.J. et al., *ApJ*, in press
- Dickinson, M. 2001, *Phil. Trans. R. Soc. London A*. 358.
- Fruchter, A.S. & Hook, R.N. 2002, *PASP*, 114, 144.
- Krist, J. & Hook, R. 2004 <http://www.stsci.edu/software/tinytim>
- Labbé, I et al. 2003, *AJ*, 125, 1107

- Lytle, D., Stobie, E. Ferro, A., & Barg, I. 1999 in ASP Conf. Ser. 172, *Astronomical Data Analysis Software and Systems VIII*, ed. D. Mehringer, R. Plante, & D. Roberts (San Francisco: ASP),445.
- Mobasher, B. et al. 2004, *HST Data Handbook for NICMOS, Revision 6.0*, Chapt. 4.1.3, <http://www.stsci.edu/hst/nicmos/documents/handbooks/DataHandbookv6/>.
- Mobasher, B. et al. 2004, *HST Data Handbook for NICMOS, Revision 6.0*, Chapt. 4.1.2, <http://www.stsci.edu/hst/nicmos/documents/handbooks/DataHandbookv6/>.
- Thompson, R.I., Storrie-Lombardi, L.J., Weymann, R.J., Rieke, M.J., Schneider, G., Stobie, E., & Lytle, D. 1999, *AJ*, 117, 17.
- Thompson, R.I., Weymann, R.J. & Storrie-Lombardi, L.J. 1999, *ApJ*, 546, 694.
- Thompson, R.I. 2003, *ApJ*, 596, 748
- Williams, R.E. et al. 1996, *AJ*, 112, 1335.

Table 1. First Half Image Positions by Visit

1	2	3	4	5	6	7	8	9	10	11	12	13	14	15	16	17	18	19	20	21	22	23	24
B	C	T	B	C	T	B	C	T	B	C	T	B	C	T	B	C	T	B	C	T	B	C	T

Table 2. Second Half Image Positions by Visit

25	26	27	28	29	30	31	32	33	34	35	36	37	38	39	40	41	42	43	44	45	46	47
R	C	L	R	R	L	R	C	L	R	C	L	R	C	L	R	L	C	L	R	R	L	R

Table 3. Data Quality Codes

bit or number	Bad Pixel	Cosmic Ray	Non Linear	Saturated
bit	8	9	12	13
number	256	512	4096	8192

Table 4. NICMOS Camera 3 distortion coefficients.

x or y	1	2	3	4	5	6	7	8	9	10
x	0.	1.0014705	0.	8.0317971E-6	1.3219373E-5	5.8285553E-6	0.	0.	0.	0.
y	0.	-8.9368516E-4	0.99853067	-1.8073393E-5	0.59911861E-7	-1.1582927E-5	0.	0.	0.	0.

Table 5. Images with special masks. The numbers and letters are the unique sections of the file names.

F110W	F160W
01bl	01ct
08me	03jy
09tf	03kj
13ap	06et
18c3	07ka
20j6	13au
27es	14d1
28im	14dn
29jr	16ve
30wj	17b8
32xe	20jb
33fh	25c4
34m8	26cm
34mq	27f0
35nt	28jc
36ot	28l1
38zd	29l1
40qs	31vp
44js	32xl
45qg	34my
...	35ny
...	36nx
...	36p0
...	38zk
...	39pe
...	40pw
...	42ht
...	43i7
...	44jz
...	45rl
...	48az

Table 6. The observed PSF parameters for the star in the NICMOS UDF images at (x,y) (819.2,597.3), a calibration star P330-E drizzled in the same way as the UDF images, and a synthetic Tiny Tim image at the camera 3 focal position used in the UDF.

Parameter	F110W UDF Star	F160W UDF Star	F110W UDF Star ^a	F160W UDF Star ^a	F110W P330-E	F160W P330-E	F110W Tiny Tim	F160W Tiny Tim
FWHM Major	0.36''	0.39''	0.38''	0.38''	0.29''	0.30''	0.29''	0.27''
FWHM Minor	0.32''	0.36''	0.35''	0.35''	0.26''	0.26''	0.25''	0.24''

^aThese values were measured for the images kindly supplied by Stiavelli, Mobasher and Bergeron. See § 7.4

Table 7. Source extraction parameters use in the NICMOS Treasury version 2.0 catalog.

Obvious parameters such as DETECT_TYPE = CCD have not been entered. The full configuration files are part of the version 2.0 Treasury archive in MAST. rmsfilter.fit refers to the rms image for a given filter such as rmsF160W.fit.

Parameter	Value	Parameter	Value	Parameter	Value
THRESH_TYPE	RELATIVE	DETECT_MINAREA	7	DETECT_THRESH	1.4
ANALYSIS_THRESH	1.4	FILTER	Y	FILTER_NAME	detec.conv
DEBLEND_NTHRESH	32	DEBLEND_MINCONT	0.001	CLEAN	Y
CLEAN_PARAM	5	MASK_TYPE	CORRECT	WEIGHT_IMAGE	rms_combfix.fit,rmsfilter.fit
WEIGHT_TYPE	RMS_WEIGHT	PHOT_APERTURES	6,11,17	PHOT_AUTOPARAMS	2.5,3.5

Table 8. A mini catalog of source parameters. See § 6.1 for a description of the parameters.

ID	ACS	SEG	X	Y	RA	DEC	PA	Elip	Rh	FWHM	stel
1	4394	605	2877.54	1797.00	53.13059235	-27.79026222	0.0000	0.8470	2.9450	4.3800	0.840
2	5109	631	2789.20	1766.72	53.13309097	-27.79101944	-23.9000	0.1540	2.0870	7.1800	0.890
3	5010	636	2764.20	1762.93	53.13379669	-27.79111481	78.0000	0.5340	4.0370	8.7800	0.910
4	4638	702	2750.66	1709.68	53.13417816	-27.79244423	-45.3000	0.4250	2.8050	5.6200	0.700
5	3460	926	2697.05	1500.98	53.13569260	-27.79766273	45.3000	0.4080	3.3700	4.1400	0.730
6	5115	627	2685.79	1769.54	53.13601303	-27.79094887	27.4000	0.3890	2.9230	7.2000	0.920
7	3871	842	2673.44	1586.07	53.13636017	-27.79553413	68.7000	0.4570	3.9490	9.2400	0.520
8	4350	774	2671.81	1643.54	53.13640594	-27.79409790	-21.0000	0.0550	2.8130	5.1000	0.980
9	3938	867	2666.78	1572.05	53.13655090	-27.79588509	17.7000	0.0380	2.5200	4.1100	0.940
10	4370	792	2661.00	1637.50	53.13671112	-27.79424858	89.8000	0.1730	2.7700	4.6100	0.430

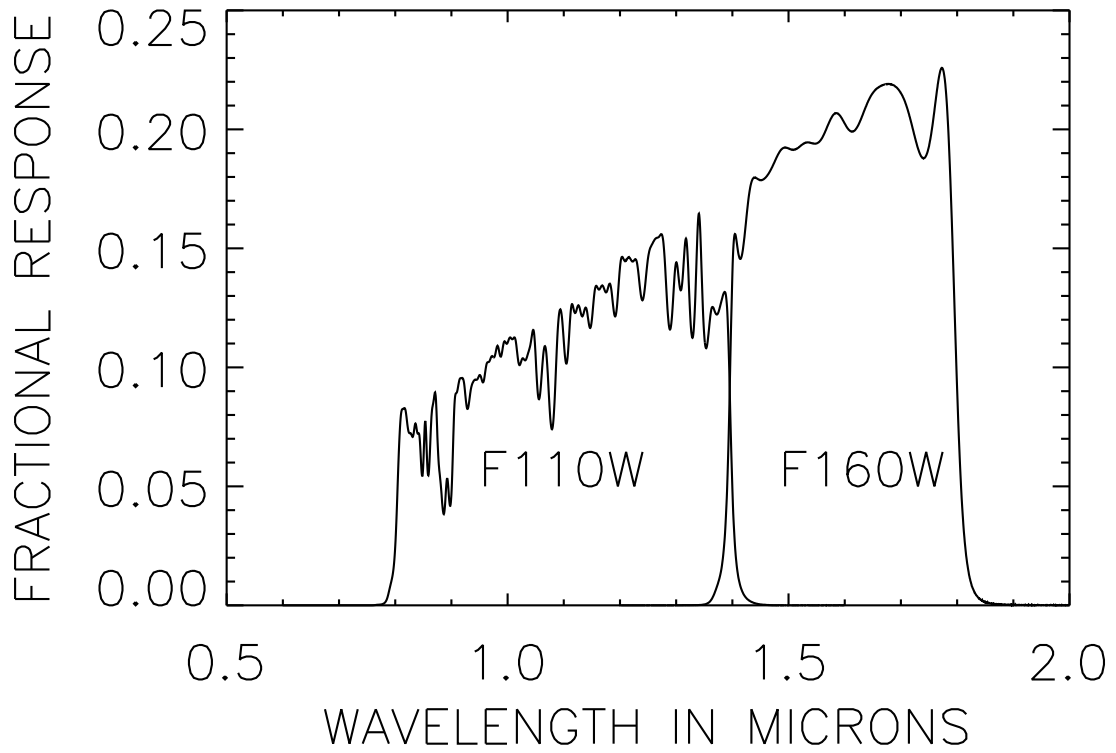


Fig. 1.— The total response functions for the NICMOS F160W and F110W filters. 100% response is equal to 1.0 on this plot.

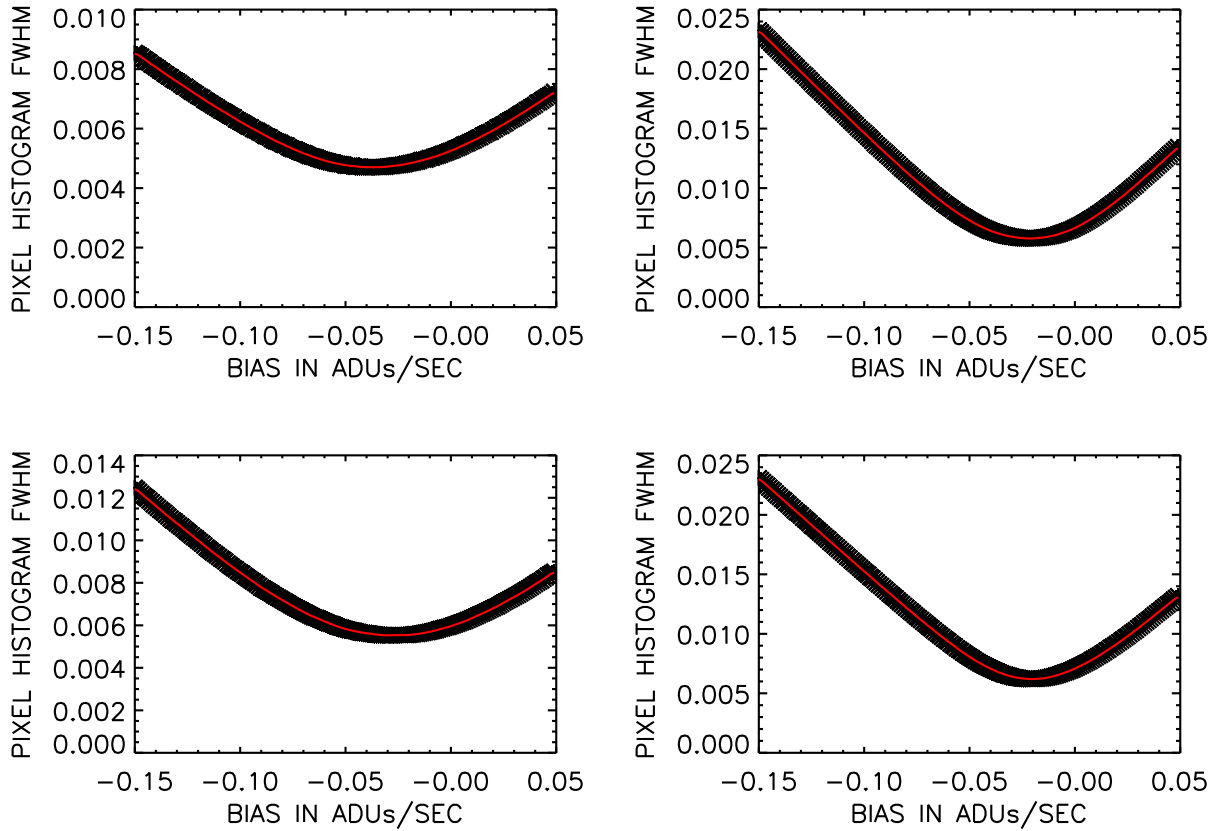


Fig. 2.— The four panels show the quadrant bias corrections in adus per second that produces the minimum variation due to flat field imprint for one of the NICMOS images. These values are taken as the appropriate quadrant bias correction. The red line shows the polynomial fit to the output and the thick black line the smoothed fit to the output. In all cases they completely overlap.

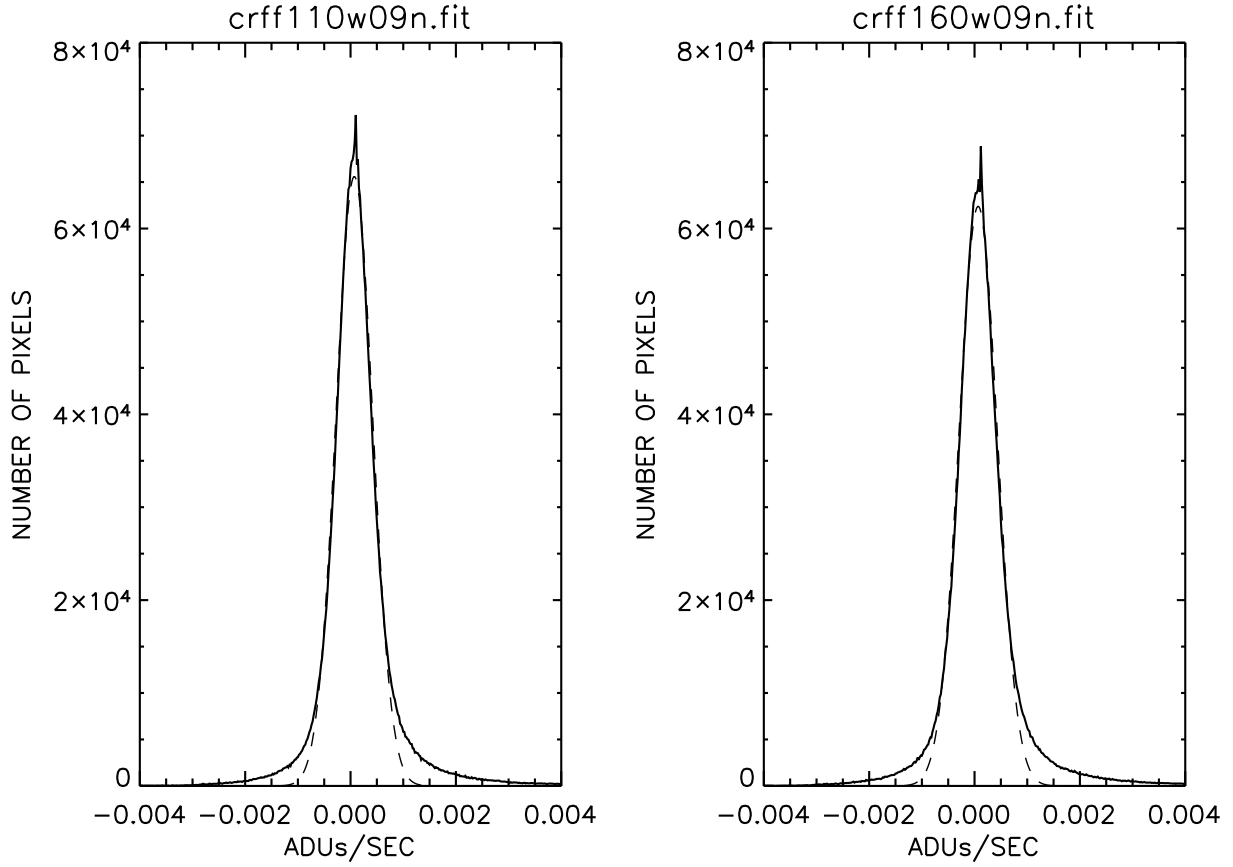


Fig. 3.— Histograms of the pixel values in the F110W (left) and F160W (right) images. The deviation from the gaussian fit on the positive side is due to the contribution of sources. The width of the gaussian is an indication of the noise in the images. See § 5.1 for a discussion of the pixel noise.

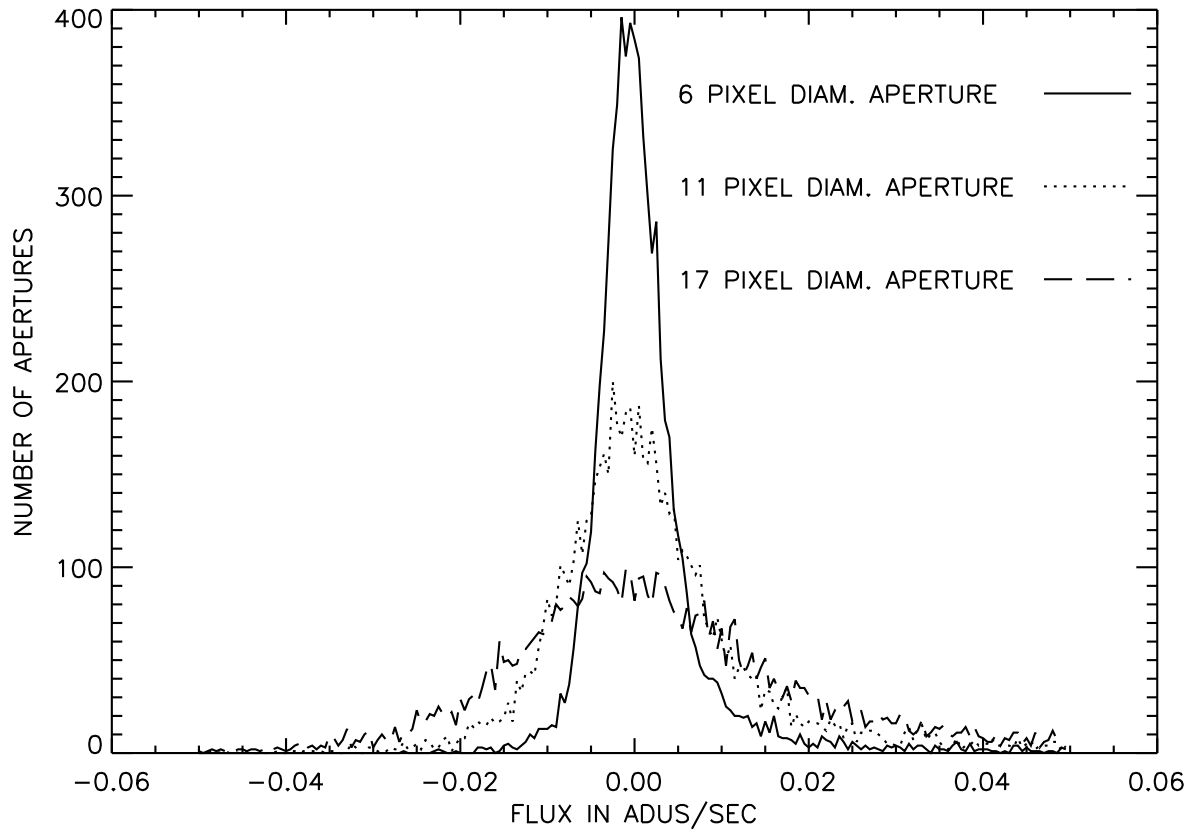


Fig. 4.— Histograms of the flux in a densely packed grid of apertures covering the UDF F110W image. The three apertures are 6, 11 and 17 pixels wide. See § 5.1 for a discussion of the aperture noise.

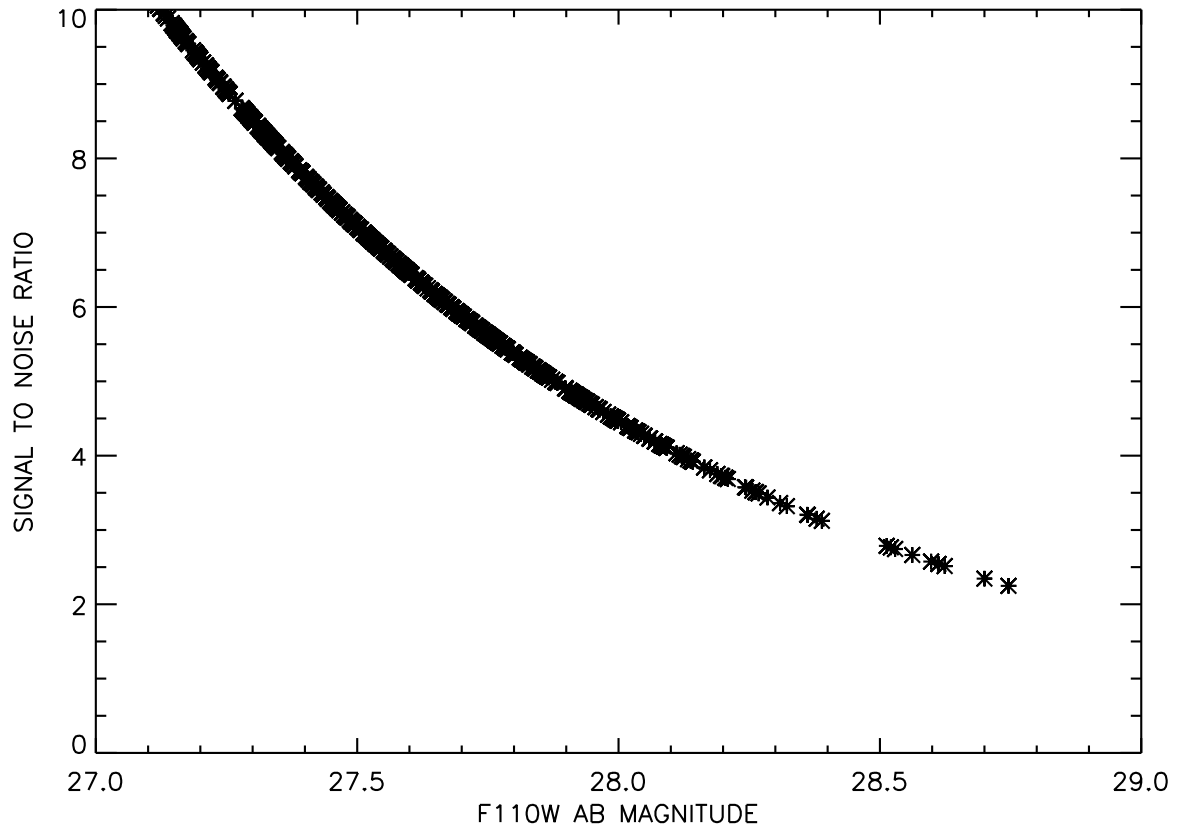


Fig. 5.— The faint end of the isophotal F110W AB magnitude versus signal to noise plot where the signal to noise is calculated from the isophotal flux and isophotal flux error returned by SE. Each source is marked by an asterisk symbol. In general the flux error returned by SE is smaller than that calculated by other means. See the discussion in § 7.1

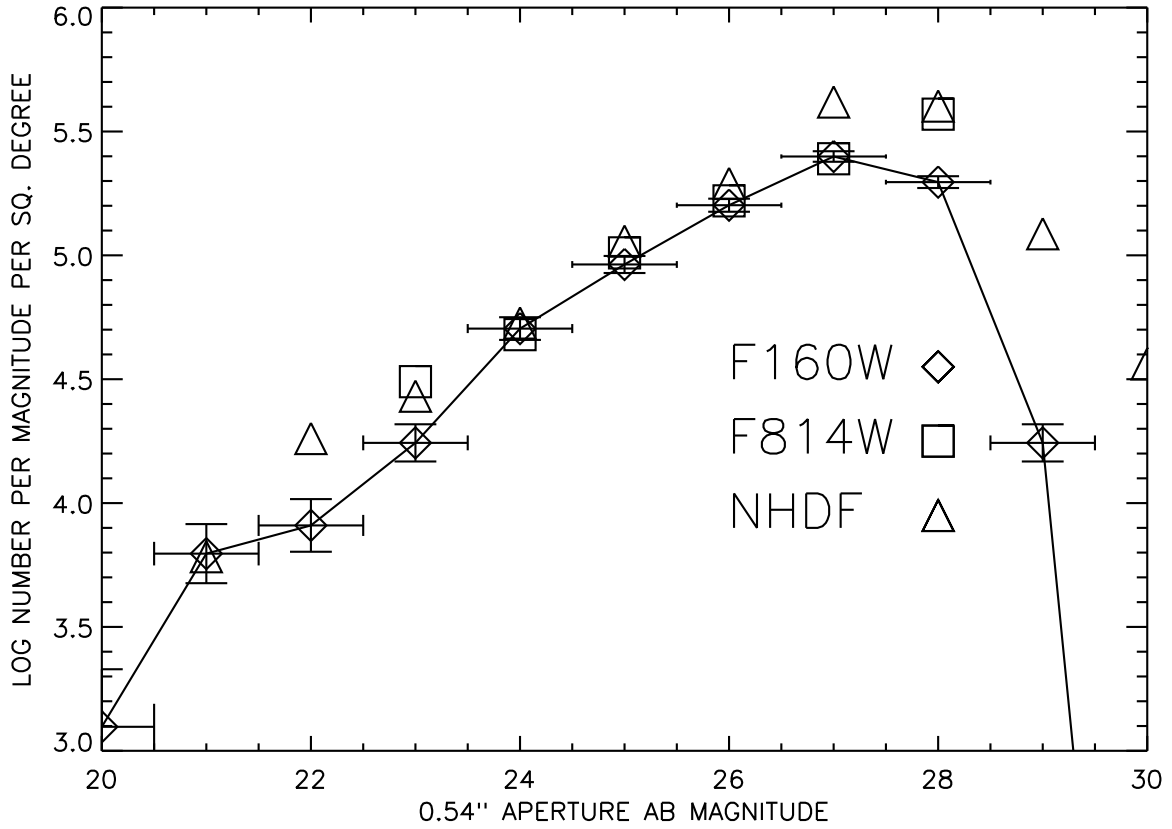


Fig. 6.— The H band (F160W) number magnitude diagram for the Ultra Deep Field. The error bars are strictly due to number statistics and do not reflect completeness or systematic errors. For comparison the NHDF F814W and F160W (NHDF) data are overplotted. The fall off at the AB magnitudes greater than 27 is partially due to the conservative nature of the source extraction used for the Treasury v2.0. catalog.